Research Square

Preprints are preliminary reports that have not undergone peer review.
They should not be considered conclusive, used to inform clinical practice,
or referenced by the media as validated information.

Characterization and Design of 3D Printed Composite Insole Fabricated by Dual-Nozzle 3D Printer Using CB-PLA and Fe-PLA Filaments

Anita Ishrat Jahan
Dong-A University
Imjoo Jung
Dong-A University
sunhee Lee
shlee014@dau.ac.kr
Dong-A University

Article

Keywords: Integrated insole, Composite structure, Dual-nozzle fused deposition modeling (FDM) 3D printing, Carbon-black polylactic acid (CB-PLA) filaments, Iron polylactic acid (Fe-PLA) filaments

Posted Date: July 13th, 2026

DOI: https://doi.org/10.21203/rs.3.rs-10200939/v1

License: This work is licensed under a Creative Commons Attribution 4.0 International License.
Read Full License

Additional Declarations: No competing interests reported.

Characterization and Design of 3D Printed Composite Insole Fabricated by Dual-Nozzle 3D Printer Using CB-PLA and Fe-PLA Filaments

Anita Ishrat Jahan[1], Imjoo Jung[2] and Sunhee Lee[1,2,*]

[1]Dept. Fashion and Textiles, Dong-A University, Busan, 49315, Rep. of Korea.

[2]Dept. Fashion Design, Dong-A University, Busan, 49315, Rep. of Korea. Correspondence and requests for materials should be addressed to S.L. (e-mail: shlee014@dau.ac.kr)

Abstract: Purpose of this study is to develop 3D printed integrated insoles fabricated using a dual-nozzle fused deposition modeling (FDM) 3D printing process. Polylactic acid (PLA) was employed as the sheath and insole material, while carbon black-filled PLA (CB-PLA) and iron-filled PLA (Fe-PLA) served as core materials. Initially, composite sheath-core structures were fabricated in both assembled and integrated forms with core diameters of 1.25, 2.50, 5.00, 7.50, and 10.00 mm and a thickness of 5.00 mm. Based on the performance evaluation of the composite structures, the integrated structure was selected for insole fabrication for its stable electrical, higher magnetic, and mechanical properties. The integrated insoles were subsequently produced with core diameters of 2.50, 5.00, 7.50, and 10.00 mm and thicknesses of 1.0, 2.5, and 5.0 mm. The 3D printed structures were characterized in terms of printing time, weight, electrical conductivity, magnetic field strength, and mechanical properties. The developed smart insole incorporated six sensing regions distributed across the primary plantar pressure zones, including the metatarsal, midfoot, and heel areas. The results demonstrated that larger core diameters and thinner insole structures enhanced electrical conductivity, with the integrated PLA/CB-PLA insole containing a 10.00 mm core and 1.0 mm thickness exhibiting the highest current of 0.10 A at 24 V. In contrast, the integrated PLA/Fe-PLA insole with the same geometry achieved a maximum magnetic field strength of 351 ± 8.84 Gs. These findings suggest that the structure, core diameter, and thickness significantly influence the electrical, magnetic, and mechanical performance for fabricating integrated insoles.

Keywords: Integrated insole, Composite structure, Dual-nozzle fused deposition modeling (FDM) 3D printing, Carbon-black polylactic acid (CB-PLA) filaments, Iron polylactic acid (Fe-PLA) filaments.

Introduction

Recent research has demonstrated that smart insoles can reliably measure plantar pressure distribution and key gait parameters. However, many existing designs still rely on externally mounted sensors, wired electronics, or layered assemblies, which can reduce comfort, limit durability, and increase system complexity. These limitations have driven growing interest in insoles with integrated sensing functionalities, where structural and functional components are combined within a single, robust structure[1-7]. Some nsoles have emerged as an important class of wearable technology for the continuous monitoring of plantar pressure, gait characteristics, and foot biomechanics. Unlike laboratory-based gait analysis systems such as force plates and motion capture systems, smart insoles offer a portable, cost-effective, and user-friendly alternative that enables long-term data acquisition in real-world environments. This portability allows gait and plantar pressure data to be collected during daily activities[8,9]. Despite these advancements, many existing smart insole systems still rely on externally mounted sensors, wired electronic components, or multi-layered assembly processes. However, these designs often suffer from reduced comfort, increased structural complexity, and a greater susceptibility to long-term mechanical failure[10]. The presence of external components can negatively affect durability and user experience, particularly under repeated loading conditions. These challenges have led to a growing research focus on developing integrated insole systems, where sensing functionality is directly incorporated into the structural body of the insole.

Fused deposition modeling (FDM) has emerged as a promising fabrication technique for insole development due to its ability to produce complex geometries[11,12]. In multi-material FDM printing, sheath-core composite structures can be manufactured as assembled structures or as integrated structures. In assembled structures, individual components are printed separately and combined using adhesives, mechanical fasteners, or thermal bonding[12-17]. In this context, But the introduction of dual-nozzle FDM systems has significantly expanded the functionality of FDM by enabling the printing of multiple materials within a single print to create an integrated structure. Integrated structures are fabricated by co-printing multiple materials in a single, continuous process[18,19]. This configuration enables the functional core to provide specific properties, such as electrical conductivity or magnetic responsiveness, while the outer sheath maintains structural integrity and mechanical stability. Furthermore, the sheath-core design enhances interfacial interactions between different material phases, thereby improving the overall performance and durability of multifunctional devices [20-21].

Conductive and magnetic composite filaments, such as carbon black polylactic acid (CB-PLA) and iron polylactic acid (Fe-PLA), offer functional properties that can be utilized for sensing applications. CB-PLA provides electrical conductivity through the formation of conductive networks within the polymer matrix [22-26]. In contrast, Fe-PLA introduces magnetic functionality [27-29]. The combination of these materials within a single printed structure allows the development of smart insoles with both electrical and magnetic capabilities. Integrating functional fillers into thermoplastic materials also presents several challenges in FDM printing. High filler content can lead to issues such as nozzle clogging, inconsistent material flow, and reduced interlayer adhesion, which may affect both print quality and mechanical performance [30,31].

This study aims to develop and evaluate multifunctional sheath-core composite structures and insoles fabricated using dual-nozzle fused deposition modeling (FDM). Polylactic acid (PLA) was used as the sheath material, while carbon black-polylactic acid (CB-PLA) and iron-polylactic acid (Fe-PLA) served as functional core materials. Initially, assembled and integrated sheath-core composite structures with various core diameters were fabricated

and characterized to investigate the effects of material composition and structural configuration on electrical, magnetic, and mechanical performance. Based on these findings, integrated insoles with different core diameters and thicknesses were designed and evaluated in terms of printing time and weight, structural integrity, electrical conductivity, and magnetic response. The study aims to identify key design parameters for the development of fully integrated insoles, providing fundamental insights for future wearable sensing, gait monitoring, rehabilitation, and healthcare applications.

Results and discussion

Actual time and weight of 3D printed assembled and integrated composite structures. Figure 1a and 1b present the printing time and weight of assembled and integrated composites with the various core sizes. The assembled structures were prepared by independently fabricating the sheath and core components, followed by their physical assembly after printing. In contrast, the integrated configurations were printed in a single printing step using a dual-nozzle FDM process where both materials were simultaneously deposited to form a continuous sheath-core structure. PLA/CB-PLA and PLA/Fe-PLA composite structures were prepared with core diameters of 1.25, 2.50, 5.00, 7.50, and 10.00 mm and thickness of 5.00 mm. In terms of printing time,as the assembled composite structures required the sheath and core components to be printed separately before assembly. Among the sheath samples, the sheath-1.25 required the longest printing time of 9 min 30 s, while the sheath-10.00 required the shortest printing time of 8 min 51 s. For the core components, the 1.25 mm cores fabricated from CB-PLA and Fe-PLA required 32 s and 34 s, respectively. As the core diameter increased to 10.00 mm, the printing times increased to 2 min 49 s for CB-PLA and 2 min 56 s for Fe-PLA. Consequently, the total printing times for the assembled composite structures were 11 min 40 s for PLA/CB-PLA-10.00 and 11 min 47 s for PLA/Fe-PLA-10.00. The printing time of the assembled structures increased with increasing core diameter due to the larger volume of functional material. The integrated composite structures showed a consistent increase in time depending on core sizes. The Integrated PLA/CB-PLA-1.25 took 12 m 1 s, followed by integrated PLA/CB-PLA-2.50, integrated PLA/CB-PLA-5.00, integrated PLA/CB-PLA-7.50, and integrated PLA/CB-PLA-10.00. The Integrated PLA/CB-PLA-10.00 required 13 m 13 s and the integrated PLA/Fe-PLA-10.00 took 13 m 27 s. The assembled composite structures required approximately 1 min less printing time than the integrated structures because the sheath and core components were fabricated separately and subsequently combined.

In terms of weight, the assembled composite structures showed an increase in total weight with increasing core diameter. For the assembled PLA/CB-PLA samples, the total weight increased from approximately 2.8 g for PLA/CB-PLA-1.25 to 3.0 g for PLA/CB-PLA-10.00. Similarly, the assembled PLA/Fe-PLA structures exhibited a gradual increase in weight from 2.8 ± 0.1 g to 3.3 g as the core diameter increased from 1.25 mm to 10.00 mm. At each core size, the PLA/Fe-PLA structures were slightly heavier than the PLA/CB-PLA composite structures. The integrated PLA/CB-PLA-1.25 had a weight of 2.6 g. In contrast, the integrated PLA/FE-PLA-1.25 was 2.7 g. As the core size increased, the weight of the samples also rose. Integrated PLA/CB-PLA-10.00 measured 2.8 g, whereas integrated PLA/Fe-PLA-10.00 weighed 3.00 g. Overall, the assembled composite structures required less printing time due to the separate fabrication of the sheath and core components. However, the integrated PLA/CB-PLA and PLA/Fe-PLA composite structures produced lighter structures than their assembled structures.

Electrical conductivity of 3D printed assembled and integrated composite structures. Figure 1c-f present the current responses of the assembled and integrated PLA/CB-PLA and PLA/Fe-PLA composite structures. All PLA/CB-PLA composite structures exhibited electrical conductivity, whereas the PLA/Fe-PLA composite structures showed negligible current flow. The structural configuration also influenced the electrical performance of the composites. The assembled PLA/CB-PLA structures exhibited slightly higher current values than the corresponding integrated structures. This behavior was attributed to the individually fabricated CB-PLA cores in the assembled structures. As a result, the assembled PLA/CB-PLA-10.00 sample exhibited the highest current value of 0.1 A at 39 V, and the integrated PLA/CB-PLA-10.00 showed a current flow of 0.1A at 45 V. Although both structures achieved similar maximum current values, the assembled structures reached this conductivity at a lower applied voltage. In contrast, the integrated structures demonstrated more uniform and stable electrical responses across all core sizes. On the other hand, the assembled composite structures showed less stability among different core sizes. Core diameters affected the conductivity of the PLA/CB-PLA composite structures. The integrated PLA/CB-PLA composite structures exhibited higher current values with increasing core diameter. At 50 V, the integrated PLA/CB-PLA-1.25, PLA/CB-PLA-2.50, PLA/CB-PLA-5.00, and PLA/CB-PLA-7.50 samples showed current values of 0.003 A, 0.02 A, 0.07 A, and 0.09 A, respectively. The integrated PLA/CB-PLA-10.00 composite structure exhibited the highest electrical performance with a current of 0.1 A at an applied voltage of 45 V. These results indicated that increasing the CB-PLA core diameter enhanced the electrical conductivity of the integrated composite structures[32].

Magnetic field strength of 3D printed assembled and integrated composite structures. Figure 1g demonstrates the magnetic field strength of the 3D printed assembled and integrated composite structures. Both assembled PLA/CB-PLA and integrated PLA/CB-PLA composite structures exhibited a constant magnetic field range across all core sizes. But the integrated PLA/CB-PLA showed a higher magnetic field than the assembled PLA/CB-PLA. The magnetic field strength of the PLA/Fe-PLA composite structures increased with core diameter, while the integrated configurations exhibited higher values than the assembled structures across the entire range of core sizes. For the assembled PLA/Fe-PLA composites, the magnetic field strength increased with core diameter, ranging from 122.67 Gs for PLA/Fe-PLA-1.25 to 136.66 Gs for PLA/Fe-PLA-10.00. The assembled PLA/Fe-PLA-2.50, PLA/Fe-PLA-5.00, and PLA/Fe-PLA-7.50 samples generated magnetic field strengths of 127.33 Gs, 130.00 Gs, and 131.00 Gs, respectively. In contrast, the integrated PLA/Fe-PLA-1.25, PLA/Fe-PLA-2.50, PLA/Fe-PLA-5.00, PLA/Fe-PLA-7.50, and PLA/Fe-PLA-10.00 samples produced magnetic field strengths of 144.33 Gs, 154.33 Gs, 164.00 Gs, 165.33 Gs, and 168.66 Gs, respectively. The integrated PLA/Fe-PLA composite structures exhibited consistently higher magnetic field strengths than the corresponding assembled structures across all core diameters. The integrated PLA/Fe-PLA-10.00 produced the maximum magnetic field of 168.66 Gs.

Compressive properties of 3D printed assembled and integrated composite structures. Figure 1h-k depict the compressive properties of 3D-printed assembled and integrated composite structures. The assembled PLA/CB-PLA composite structures supported an average load of 8.57 ± 1.18 kN at 59.27 % strain, and the Assembled

PLA/Fe-PLA endured 6.52 ± 2.37 kN at 45.38 ± 14.15 % strain. For the assembled PLA/CB-PLA composite structures, the curves suddenly dropped after reaching 7.38 kN at 47.16% strain. A similar curve drop occurred in the assembled PLA/Fe-PLA after 5.25 kN at 33.91% strain. In both cases, this happened because the interfacial bonding between the two parts was weak. Both assembled PLA/CB-PLA composite structures and the assembled PLA/Fe-PLA composites showed an irregular S-S curve because of the early breakage of the composites. The integrated PLA/CB-PLA composite structures showed a load-bearing capacity of 8.81 ± 2.04 kN at 66.23 ± 5.48 % strain on average. The integrated PLA/Fe-PLA composite structures exhibited an average of 9.1 ± 1.46 kN at 66.62 ± 5.83 % strain overall. The integrated PLA/Fe-PLA composite structures showed higher compressive strength and resistance to deformation. **Table 1** shows the morphology image and the changed ratio of assembled and integrated composite structures after the compression test. The composite structures showed differences in their mechanical performance because of the use of different types of filaments and different printing methods. The integrated composite structures exhibited significantly higher load-carrying capacity and more uniform deformation. The enhanced performance was primarily associated with the continuous bonding formed during the dual-nozzle co-printing process, which facilitated efficient stress transfer across the interface and reduced the presence of internal voids. Morphological analysis revealed that the sheath and core remained firmly bonded in the integrated structures even after high compressive stress, while interfacial separation occurred in the assembled structures under similar loading conditions. As a result, integrated composite structures exhibited stronger mechanical strength and bonding quality. The assembled composite structures exhibited irregular S-S curves with sudden stress drops, likely from the separate fabrication of the components. Consequently, the assembled structures showed lower mechanical stability. In comparison, the integrated composite structures exhibited stable S-S curves with uniform load transfer throughout the structure. Across the various core diameters, both assembled PLA/CB-PLA and assembled PLA/Fe-PLA composite structures exhibited sudden drops. In contrast, the integrated PLA/CB-PLA composite structures showed a load-carrying capacity with increasing core diameter. Compressive stress increased from 5.3 kN to 9.41 kN for the integrated PLA/CB-PLA-1.25 to the integrated PLA/CB-PLA-10.00. On the other hand, the integrated PLA/Fe-PLA-1.25 composite structure resisted compressive stress of 7.54 kN, and the stress value rose with each increase in core diameter. The integrated PLA/Fe-PLA-10.00 showed the highest compressive stress of 10.22 kN. Overall, the results indicated that the integrated composite structures provided higher compressive strength, deformation stability, and bonding integrity. The stable behavior was caused by increased stress transfer across the interface of composite structures and gap reduction with the help of continuous bonding during dual-nozzle printing. The S-S curves of assembled composite structures showed some fluctuations and were relatively unstable. These results validated that the printing approach was responsible for compressive response and the dual-nozzle integrated printing facilitated the enhancement of structural strength.

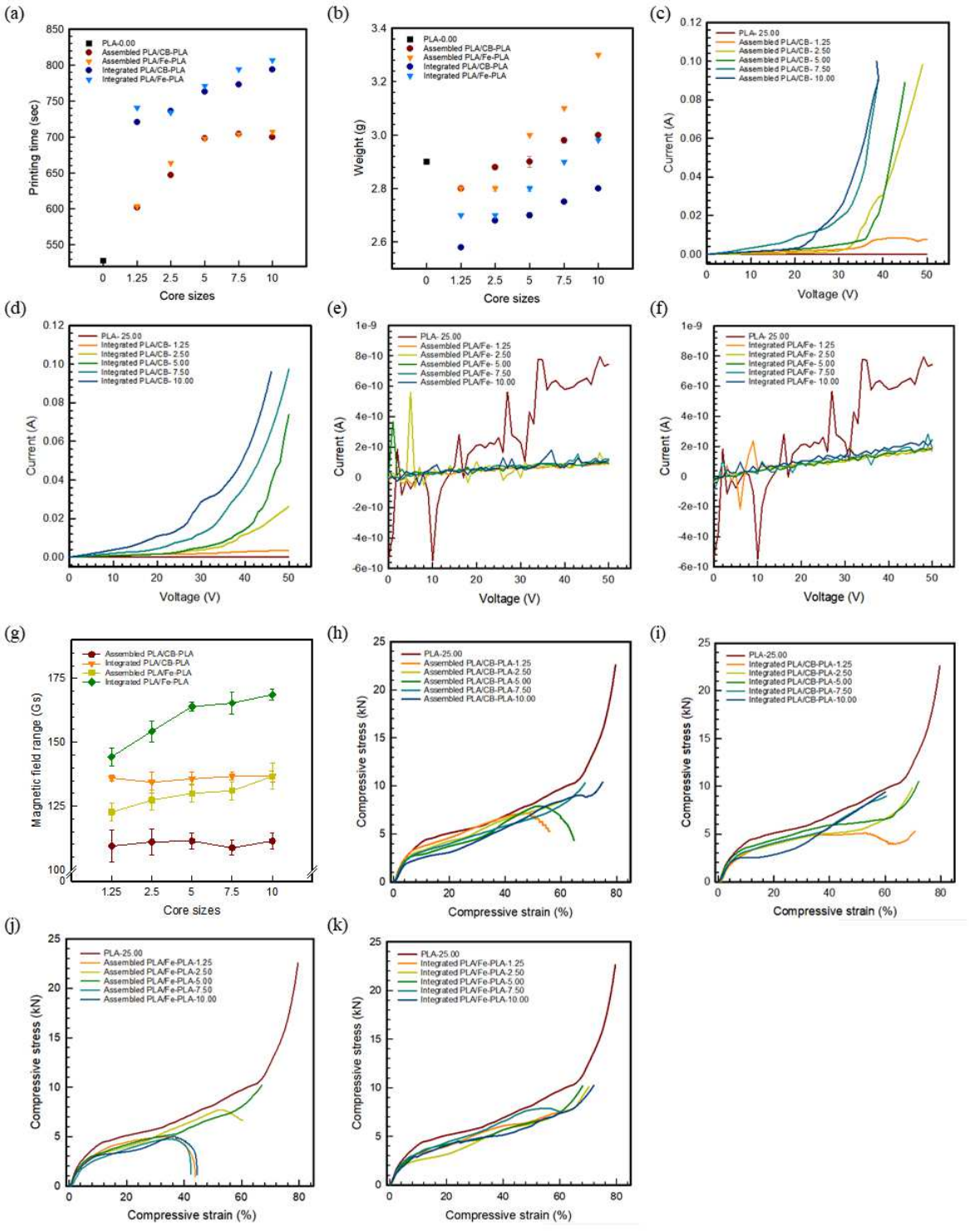


Fig. 1. (**a**) Actual printing time of 3D printed assembled and integrated composite structures. (**b**) Weight of 3D printed assembled and integrated composite structures. (**c**) Electrical properties of Assembled PLA/CB-PLA. (**d**) Electrical properties of Integrated PLA/CB-PLA. (**e**) Electrical properties of Assembled PLA/Fe-PLA. (**f**) Electrical properties of Integrated PLA/Fe-PLA. (**g**) Magnetic field strength of assembled and integrated composite structures (**h**) S-S curves of Assembled PLA/CB-PLA. (**i**) S-S curves of Integrated PLA/CB-PLA. (**j**) S-S curves of Assembled PLA/Fe-PLA. (**k**) S-S curves of Integrated PLA/Fe-PLA.

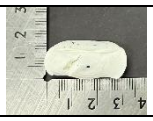
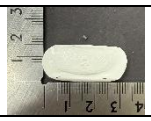
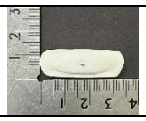
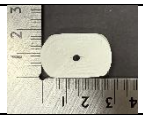
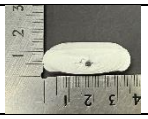
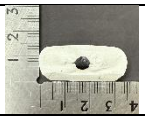
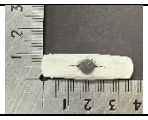
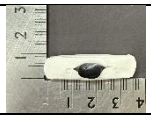
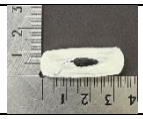
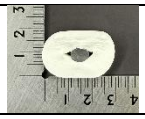
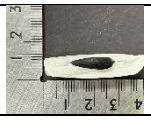
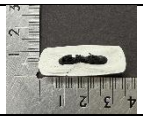
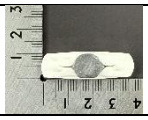
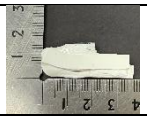
Core		Sheath	PLA/CB-PLA		PLA/Fe-PLA	
			Assembled	Integrated	Assembled	Integrated
0.00			-	-	-	-
Changed ratio	Width (%)	52.00 ± 0.00	-	-	-	-
	Length (%)	72.00 ± 0.00				
1.25						
Changed ratio	Width (%)		20.50 ± 11.35	16.8 ± 11.79	14.00 ± 14.14	22.40 ± 3.58
	Length (%)		30.00 ± 15.14	40.00 ± 0.00	28.00 ± 16.97	39.20 ± 9.12
2.50						
Changed ratio	Width (%)		26.67 ± 4.61	21.60 ± 13.14	32.00 ± 0.00	36.00 ± 5.65
	Length (%)		45.33 ± 9.23	32.00 ± 5.66	52.00 ± 0.00	52.00 ± 11.31
5.00						
Changed ratio	Width (%)		36.00 ± 4.00	16.80 ± 13.38	42.00 ± 2.83	25.00 ± 5.03
	Length (%)		52.00 ± 5.56	44.00 ± 22.62	44.00 ± 22.62	44.00 ± 3.26
7.50						
Changed ratio	Width (%)		38.67 ± 14.04	20.00 ± 18.54	24.00 ± 4.00	27.20 ± 5.21
	Length (%)		62.67 ± 4.61	49.33 ± 8.32	34.67 ± 10.07	39.2 ± 3.34
10.00						
Changed ratio	Width (%)		16.00 ± 0.00	26.40 ± 12.19	37.33 ± 8.33	29.33 ± 4.61
	Length (%)		20.00 ± 0.00	50.00 ± 14.21	50.67 ± 16.16	24.00 ± 4.00

Table 1. Morphology image and the changed ratio of 3D printed composite structures.

Actual time and weight of 3D printed integrated insole. Based on the overall performance of the composite structures, the integrated fabrication strategy was adopted to develop the insoles. The integrated insoles were produced with core diameters of 2.50, 5.00, 7.50, and 10.00 mm and thicknesses of 1.00, 2.50, and 5.00 mm to evaluate the influence of geometric parameters on their functional performance. Figure 2a and 2b present the actual printing time and weight of integrated PLA/CB-PLA and PLA/Fe-PLA insoles. As for the integrated PLA/CB-2.5 with a thickness of 1.00 mm required 5 min 11 sec, and the integrated PLA/CB-PLA-10.00 with a thickness of 1.00 mm, needed 8 min 37 sec. As the core size increases, the printing time also increases. With the thickness, the integrated PLA/CB-PLA- 5.0 insoles with thickness 1.00 mm required 6 min 15 sec and with thickness 5.00 mm thickness 28 min 40 sec. For both integrated PLA/CB-PLA and PLA/Fe-PLA insoles, the printing time increased with increasing core diameter and thickness. This behavior was consistently observed across all thicknesses and core diameters for both integrated PLA/CB-PLA and PLA/Fe-PLA structures as

identical modeling and slicing parameters were employed with the core material being the only variable. The integrated PLA/CB-2.5 with a thickness of 1.00 mm, weighed 0.71 ± 0.01 g, and the integrated PLA/CB-PLA-2.5 with a thickness of 5.00 had a weight of 3.62 ± 0.01 g. The measured weights of the integrated insoles followed trends similar to printing time. However, the integrated PLA/Fe-PLA insoles exhibited higher weights than the integrated PLA/CB-PLA insoles owing to the greater density of Fe-PLA compared with CB-PLA.

Electrical properties of 3D printed integrated insole. Figure 2c-j illustrates the electrical properties of the integrated PLA/CB-PLA and PLA/Fe-PLA insoles evaluated through I-V measurements at different core diameters and insole thicknesses. The PLA/CB-PLA-2.50 insole with a thickness of 1.00 mm showed a current value of 0.006 A and an increase in core size of 5.00 mm increased the current to about 0.009 A at 20 V. A further increase in core size to 7.50 mm produced current values close to 0.02 A. The highest current was observed at the 10.00 mm core about 0.03 A at 20 V for the 1.00 mm thickness. Increasing the thickness from 1.00 mm to 5.00 mm reduced the current. But the 2.5 mm-thick insoles generally exhibited slightly higher current values than the 1.0 and 5.0 mm insoles across all the core sizes. For the integrated PLA/CB-PLA insole with a 2.5 mm core diameter, the 2.50 mm-thick insole exhibited the highest current of 0.0122 A at 20 V, followed by the 5.00 mm-thick insole (0.0089 A) and the 1.00 mm-thick insole (0.0060 A).

In contrast, the PLA/Fe-PLA insoles with core sizes of 2.50, 5.00, 7.50, and 10.00 mm exhibited low current flow across the applied voltage, remaining close to zero and within the range of 10^{-9} A. Increasing the thickness did not significantly change the current behavior. Overall, the PLA/Fe-PLA insoles exhibited negligible current regardless of core size or thickness. Instead, the Fe-PLA core remains electrically insulating regardless of its size or thickness.

Magnetic field strength of 3D printed integrated insole. Figure 2k presents the magnetic field strengths of the integrated PLA/CB-PLA and PLA/Fe-PLA insoles, together with their corresponding regression analyses. The PLA/CB-PLA smart insoles showed relatively low magnetic field strength across all core sizes. The values remained nearly constant, around 166-170 Gs for the 5.00 mm thickness, 237-242 Gs for the 2.50 mm thickness, and 305-310 Gs for the 1.00 mm thickness. Changes in thickness affected the magnetic behavior of the PLA/CB-PLA smart insoles due to the influence of the G2 magnet used to quantify the magnetic field strength. This indicated PLA/CB-PLA did not contribute to the magnetic field response.

The PLA/Fe-PLA-2.50 insole showed a magnetic field strength of 315.67 ± 4.63 Gs at 1.00 mm thickness. Increasing the thickness to 5.00 mm at the same core size reduced the magnetic field strength to 185.15 ± 4.62 Gs. For the PLA/Fe-PLA-10.00 insole, a magnetic field strength of 351.60 ± 8.43 Gs was observed at 1.00 mm thickness and with increasing thickness to 5.00 mm, it was reduced to 315.66 ± 4.63 Gs. Overall, the magnetic field strength of the PLA/Fe-PLA insoles increased with increasing core size from 2.50 mm to 10.00 mm, and decreasing thickness led to higher magnetic field strength. Thickness significantly influenced the magnetic field strength of the integrated PLA/Fe-PLA insoles. Thinner samples exhibited higher magnetic field strength at the same core size, while thicker samples showed reduced values. This reduction is mainly due to enhanced magnetic flux attenuation with increasing thickness, resulting in a diminished effective magnetic field[33,34]. Overall, the

regression analysis demonstrated that the integrated PLA/CB-PLA insoles showed minimal magnetic field strength. The integrated PLA/Fe-PLA insoles illustrated magnetic response with core diameter and thickness.

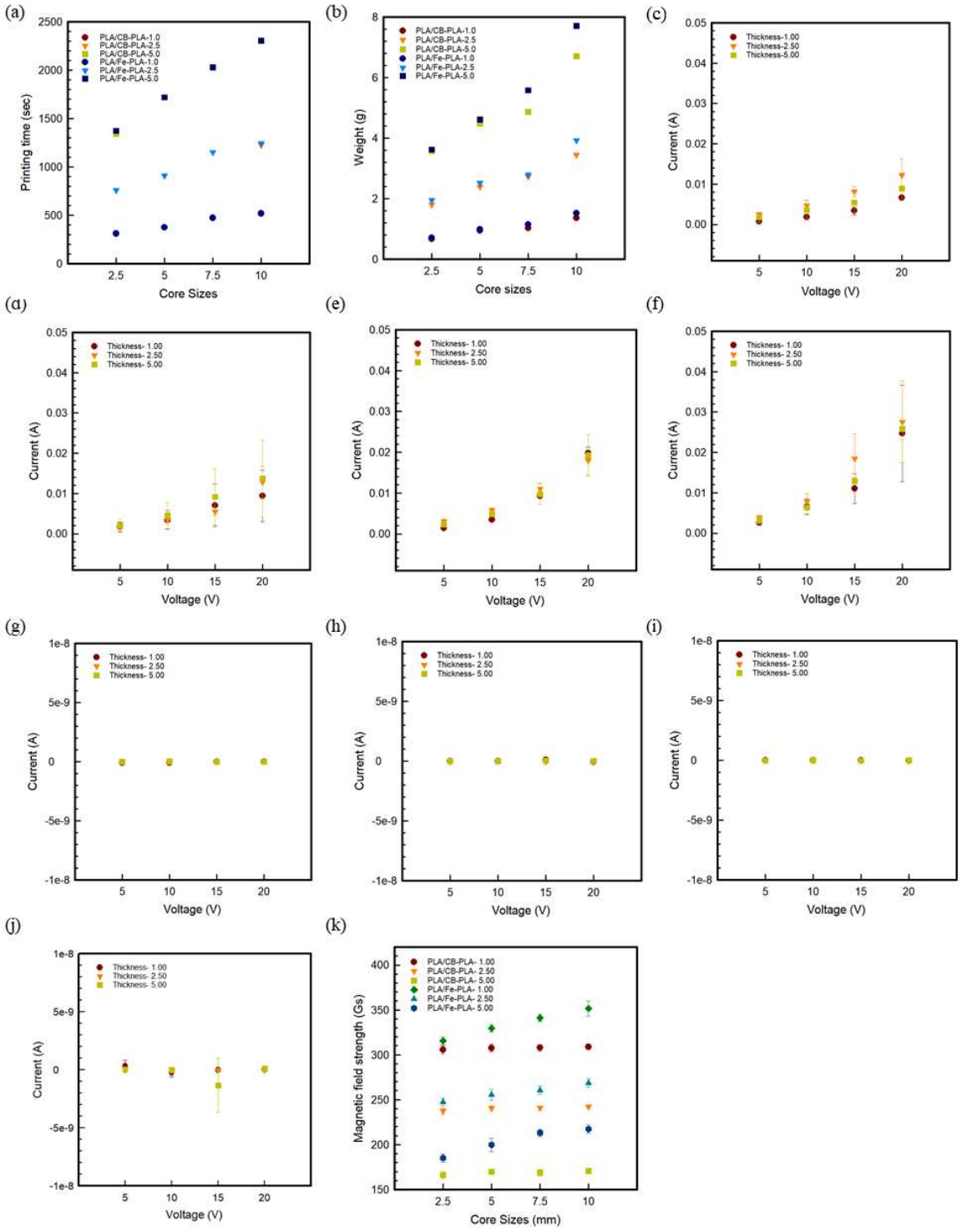


Fig. 2. (**a**) Actual printing time of 3D printed integrated insole. (**b**) Weight of 3D printed integrated insole. (**c**) Electrical properties of integrated insole PLA/CB-PLA- 2.50. (**d**) Electrical properties of integrated insole PLA/CB-PLA- 5.00. (**e**) Electrical properties of integrated insole PLA/CB-PLA- 7.50. (**f**) Electrical properties of integrated insole PLA/CB-PLA- 10.00 (**g**) Electrical properties of integrated insole PLA/Fe-PLA- 2.50. (**h**) Electrical properties of integrated insole PLA/Fe-PLA- 5.00. (**i**) Electrical properties of integrated insole PLA/Fe-PLA- 7.50. (**j**) Electrical properties of integrated insole PLA/Fe-PLA- 10.00 (**k**) Magnetic field strength of 3D printed integrated insole.

Conclusion

This study investigated the modeling, printing, and analysis of composite structures with various core sizes as well as insoles with various core sizes and thicknesses using dual-nozzle FDM printing. By adopting functional materials within a single printing process, this study aimed to address the limitations associated with assembly complexity. The integrated structures exhibited simplified fabrication while printing the samples, along with stable and uniform performance.

A comparative analysis of assembled and integrated composite structures was conducted. The integrated structures exhibited enhanced mechanical performance with a maximum compressive strength of 9.41 kN and improved structural integrity. Furthermore, larger CB-PLA core diameters led to higher electrical conductivity, whereas Fe-PLA cores produced stronger magnetic fields. Consequently, the integrated configuration was chosen for the development of the smart insoles.

Based on the integrated composite structures, fully integrated insoles were successfully fabricated using dual-nozzle FDM. Sensor regions were positioned in six biomechanically relevant areas of the insole, including the heel, midfoot, and metatarsal regions. The printed integrated insoles showed consistent morphology across all core sizes and thicknesses. The electrical results indicated that the integrated PLA/CB-PLA-10.00 insole demonstrated the highest conductivity, with the 2.50 mm thick insole recorded a current of 0.028 ± 0.01 A at an applied voltage of 20 V. The integrated PLA/Fe-PLA insoles did not demonstrate electrical responsiveness, but they produced a stronger magnetic field. A magnetic field strength of 351.60 ± 8.43 Gs was observed for the integrated PLA/Fe-PLA-10.00 insole with a thickness of 1.00 mm. Increasing core diameter improved magnetic field strength, whereas increasing insole thickness reduced magnetic intensity due to attenuation effects. The study showed that variations in core size and thickness can be controlled to achieve desired multifunctional performance in integrated smart insole structures.

Finally, this study proved that dual-nozzle FDM printing of PLA-based composite filaments offers a practical and scalable method for producing multifunctional insoles with dependable mechanical strength and embedded sensing capabilities. The integrated sheath-core structures enabled improved mechanical durability, with electrical and magnetic properties. The methodology and insights gained from this study support the progress of FDM-based wearable technologies and establish a base for future research on fully integrated footwear. The integrated structure improved suitability for wearable applications by eliminating post-printing assembly and adhesive bonding, thereby reducing structural complexity and simplifying the fabrication process.

Furthermore, the integrated dual-nozzle fabrication strategy demonstrated in this study may provide future opportunities for industrial applications and commercialization in personalized footwear and wearable monitoring devices.

Methods

Materials. Three types of polylactic acid filaments were selected to fabricate composite structures and the smart insoles. These included polylactic acid (PLA white, Ultimaker B.V., Netherlands), carbon black-polylactic acid (CB-PLA, composite conductive PLA, Protopasta Co. Ltd., USA), and iron polylactic acid (Fe-PLA, composite Iron PLA, Protopasta Co. Ltd., USA) illustrates in **Figure 3a**. All filaments had a diameter of 2.85 mm. The

measured densities were 1.24 g/cm³ for PLA, 1.15 g/cm³ for CB-PLA, and 1.83 g/cm³ for Fe-PLA. Ultimaker S3 (Ultimaker B.V., Netherlands) dual-nozzle FDM 3D printer was used. From the filament analysis, energy-dispersive X-ray spectroscopy (EDS) analysis confirmed that carbon and oxygen were the primary elements in PLA with atomic percentages of 62.33% and 36.33%, respectively. CB-PLA also contained carbon and oxygen as the major elements. The carbon atomic percentage increased to 69.63%, which confirmed the presence of carbon black particles within the PLA matrix. In addition, Fe-PLA filament contained approximately 51% carbon, 38% oxygen, and 11% iron[27]. For the first heating cycle, PLA exhibited a T_g of 68.4 °C and a T_m of 150.5 °C, whereas CB-PLA showed lower thermal transition temperatures, with a T_g of 61.9 °C and a T_m of 148.5 °C. Similarly, Fe-PLA exhibited a T_g of 61.6 °C and a T_m of 148.2 °C[27]. TGA analysis revealed that PLA underwent almost complete decomposition between 300 and 380 °C, with a residual mass of 1.8%. CB-PLA exhibited a total weight loss of 81.2% and remained 13.0% residual mass of 18.8% due to the carbon black filler. The Fe-PLA filament contained approximately 51% carbon, 38% oxygen, and 11% iron[27]. Based on the extrusion test, 225 °C for CB-PLA and 180 °C for Fe-PLA were identified as the optimal printing temperatures, yielding extruded filament diameters of 414.83 ± 2.29 µm and 581.54 ± 8.02 µm, respectively. These temperatures produced filament dimensions closest to the nozzle diameter.

Preparation of Assembled and integrated composite structures. Figure 3b presents the PLA/CB-PLA and PLA/Fe-PLA composite structures fabricated using a dual-nozzle FDM 3D printer (Ultimaker S3, Ultimaker B.V., Netherlands) under two different fabrication methods. The modeling and slicing process of the assembled PLA/CB-PLA, integrated PLA/CB-PLA, assembled PLA/Fe-PLA, and integrated PLA/Fe-PLA composite structures are also illustrated. The assembled method involves printing the sheath and core components separately and subsequently joining them. Secondly, the integrated method involves both materials in a single process. Accordingly, four types of samples were prepared, which were assembled PLA/CB-PLA, integrated PLA/CB-PLA, assembled PLA/Fe-PLA, and integrated PLA/Fe-PLA. The sheath dimensions were maintained at a diameter of 25 mm and a thickness of 5.00 mm, each having core diameters of 1.25 mm, 2.50 mm, 5.00 mm, 7.50 mm, and 10.00 mm. Modeling was done with Autodesk Fusion (Autodesk Inc., USA), and the 3D models of composite structures were saved in *.stl files. Ultimaker Cura 5. 9.0 software (Ultimaker B.V., Netherlands) was used to prepare the model slicing, where *.stl files were converted into printable *.ufp files within the slicing program. The printing temperatures were set to 200 °C for PLA, 225 °C for CB-PLA, and 180 °C for Fe-PLA. A consistent bed temperature of 60 °C was maintained to support proper adhesion during the printing process. Nozzle 1 was used for the sheath, and nozzle 2 was used for the core. 0.4 mm AA nozzles were used for printing. The print speed was set to 100 mm/s for all samples. A zigzag infill pattern with 100% infill density was applied across all the samples to ensure full volume and uniform material distribution.

Integrated smart insoles preparation. Based on the overall performance of the composite structures, the integrated structure was adopted for insole fabrication due to its superior structural stability and improved functional properties. In **Figure 3c,** based on findings from our previous study, six anatomically relevant regions were identified for sensor integration within the insole, encompassing the metatarsal, midfoot, and heel areas. These regions were selected because they correspond to the major load-bearing zones of the foot, where elevated

plantar pressures are consistently observed during both standing and gait activities[35]. The integrated insoles were designed with four core diameters of 2.50, 5.00, 7.50, and 10.00 mm and three thicknesses of 1.00, 2.50, and 5.00 mm to systematically examine the effects of geometric design parameters on their performance. The insoles were fabricated using optimized printing parameters while maintaining the same processing conditions as those used for the composite structures, with the exception of the infill density (10%). Furthermore, the insoles were manufactured without top and bottom layers to achieve the desired structural configuration.

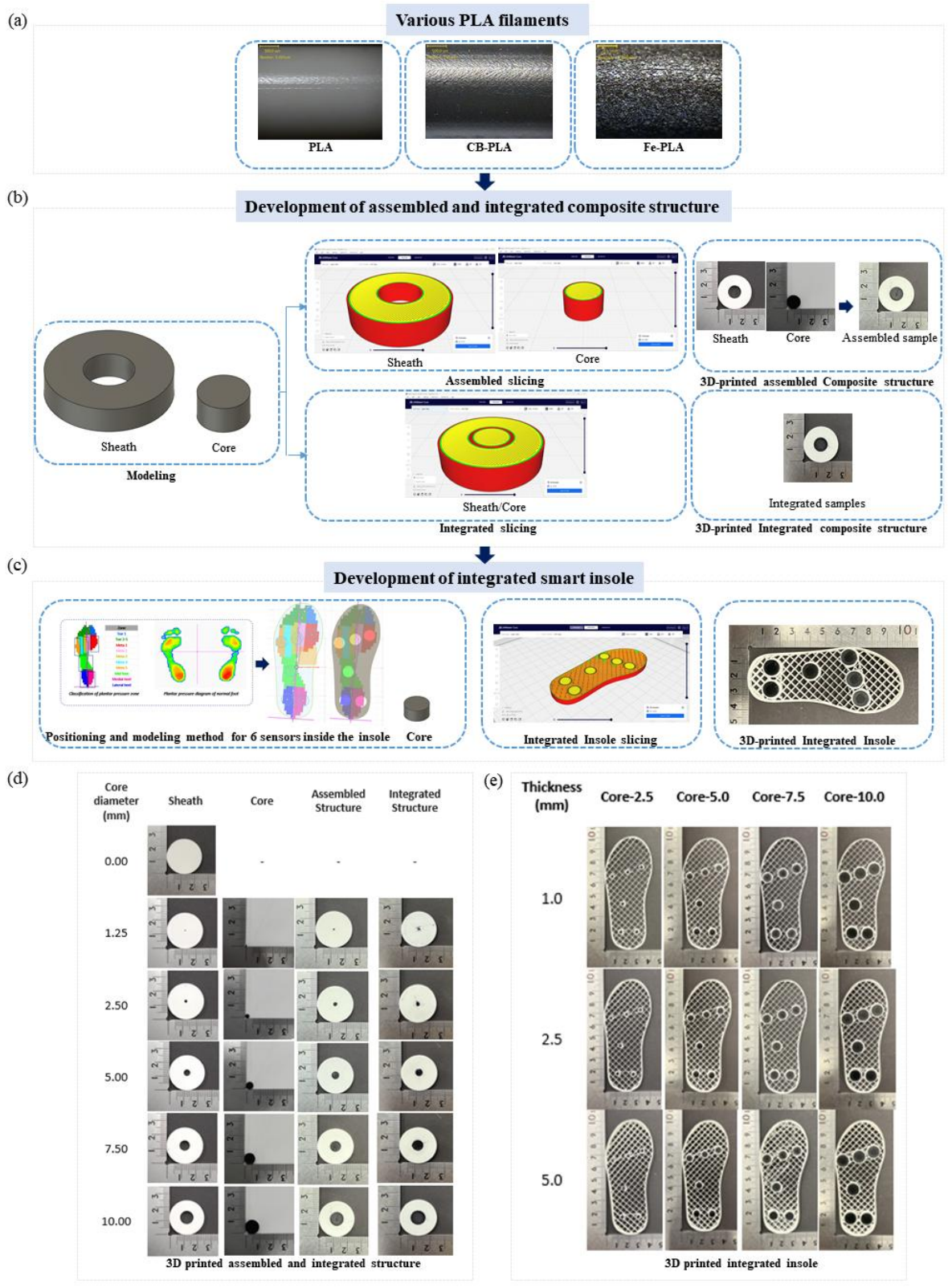


Fig 3. (**a**) Various PLA filament samples. (**b**) Sample preparation method of 3D printed assembled and integrated composite structures. (**c**) 3D printed integrated smart insole preparation process. (**d**) 3D printed assembled and integrated composite structure. (**e**) 3D printed integrated insole.

Characterization

In this study, the 3D-printed assembled and integrated composite structures were characterized using the following analytical methods. Actual printing time and weight. The printing time of each composite structure was recorded directly from the Ultimaker S3 3D printer and reported in minutes (min) and seconds (s). The weight of the printed composite structures was determined using an electronic balance (PAG114, OHAUS, USA). To ensure measurement reliability, each specimen was weighed three times, and the mean value was calculated. The average and standard deviation values were reported in grams (g). Electrical properties were measured using a 2450 source meter (Keithley 2450 Source Measure Unit, Tektronix Inc., USA) configured in a two-probe mode. The voltage was swept from -1 V to 50 V in 0.1 V increments. The results were analyzed to evaluate the electrical conductivity using the I-V curves. The magnetic field strength of the fabricated composite structures was evaluated using a Gauss meter (GS-100D2, LANDTEK, China). The measurement range was 0-2000 Gs, enabling detection of the field variation within composite structures. General magnets (G2) were used to quantify the field strength generated by the composite structures. G2 magnets' magnetic field ranges were 284.8 ± 39.7 Gs [27]. Compressive properties. The compressive properties of the fabricated composite structures were measured using a universal testing machine (Instron 5567, Instron, USA). The test was conducted under controlled conditions with an initial load of 5 N and a crosshead speed of 25 mm/min. These parameters were selected to ensure stable pressure and accurate evaluation of the mechanical behavior of the composite structures until breakage. After the test, the changed ratio of length and width was calculated using the diameter of the composite structure as the baseline, as shown in equation (1) for the length ratio and equation (2) for the width ratio.

$$\text{Ratio of Length } (\%) = \left(\frac{L_0 - L_1}{L_0}\right) \times 100 \quad (1)$$

Where L_0 (mm) represents the composite structure's original diameter, and L_1 (mm) represents the changed length measurement of the composite structures.

$$\text{Ratio of Width } (\%) = \left(\frac{W_0 - W_1}{W_0}\right) \times 100 \quad (2)$$

Where W_0 (mm) represents the composite structure's original diameter, and W_1 (mm) represents changed width measurement of the composite structure.

Secondly, the actual printing time, weight, and magnetic field strength of the 3D-printed integrated insoles were characterized using the same experimental procedures and analytical methods applied to the assembled and integrated composite structures. During Electrical properties measurements, the applied voltage was swept from 0 V to 25 V in 0.1 V intervals. The measurements were performed for each 3D-printed integrated PLA/CB-PLA and PLA/Fe-PLA integrated insole. For each insole, all six sensor cores were measured individually, and each measurement was repeated three times. The average values and standard deviations were calculated. At specific fixed point current values were evaluated at applied voltages of 5 V, 10 V, 15 V, and 20 V for each core size and insole thickness. The magnetic field strength of the 3D-printed integrated insoles was evaluated using the same experimental procedure described for the assembled and integrated composite structures.

Data availability

The datasets used and/or analyzed during the current study available from the corresponding author S. Lee (shlee014@dau.ac.kr) on reasonable request.

References

1. Samarentsis, A. G. et al. A 3D-Printed Capacitive Smart Insole for Plantar Pressure Monitoring. Sensors. **22** (24), 9725 (2022).
2. Vu, L.T., Bottin-Noonan, J., Armitage, L., Alici, G. & Sreenivasa, M. 3D-Printed Insole for Measuring Ground Reaction Force and Center of Pressure During Walking. Sensors. (Basel) **25**, (2025).
3. Binelli, M.R. et al. Digital manufacturing of personalised footwear with embedded sensors. Scientific Reports. **13**, 1962 (2023).
4. Gothard, A.T., Hott, J.W. & Anton, S.R. Dynamic Characterization of a Low-Cost Fully and Continuously 3D Printed Capacitive Pressure-Sensing System for Plantar Pressure Measurements. Sensors. **23**, 8209 (2023).
5. Danko, M., Sekac, J., Dzivakova, E., Zivcak, J., Hudak, R. 3D printing of individual running insoles–A case study. Orthopedic Research and Reviews. **15**, 105-118 (2023).
6. Wang, L., Tang, F., Chen, J. Multi-material additive manufacturing via fused deposition modeling 3D printing: A systematic review on the material feeding mechanism. Proceedings of the Institution of Mechanical Engineers, Part E: Journal of Process Mechanical Engineering. **239** (6), (2024).
7. Nazir, A. et al. Multi-material additive manufacturing: A systematic review of design, properties, applications, challenges, and 3D printing of materials and cellular metamaterials. Materials & Design, **226**, 111661 (2023).
8. Espalin, D., Ramirez, J., Medina, F. & Wicker, R. Multi-material, multi-technology FDM: exploring build process variations. Rapid Prototyping Journal. **20**, (2014).
9. Massaroni. C., Saroli, V., Aloqalaa Z., Presti, D. & Schena, E. Extrusion-Based Fused Deposition Modeling for Printing Sensors and Electrodes: Materials, Process Parameters, and Applications. SmartMat. **6**, (2025).
10. Rafiee, M., Farahani, R.D. & Therriault, D. Multi-material 3D and 4D printing: a survey. Advanced science. **7** (12), 1902307 (2020).
11. Chen, H., Guo, L., Zhu, W. & Li, C. Recent Advances in Multi-Material 3D Printing of Functional Ceramic Devices. Polymers. **14** (21), 4635 (2022).
12. Willemstein, N., Sridar, S., Kooij, H. & Sadeghi, A. A feasibility study on using soft insoles for estimating 3D ground reaction forces with incorporated 3D-printed foam-like sensors. Wearable Technologies. **6**, (2025).
13. Alegria, M., Ballesteros, M. & Cruz-Ortiz, D. A wireless instrumented insole for monitoring plantar pressure during human locomotion. Sensing and Bio-Sensing Research. **47**, 100752 (2025).
14. Seo, M., Shin, M. J., Park, T. S. & Park, J.H. Clinometric gait analysis using smart insoles in patients with hemiplegia after stroke: pilot study. JMIR mHealth and uHealth. **8**(9), e22208 (2020).
15. D'Arco, L., Wang, H. & Zheng, H. Integration of smart insoles for gait assessment in exoskeleton-assisted rehabilitation. Scientific Reports. **15**(1), 28350 (2025).
16. Jonnala, U.K. & Kumar, Y.R. Design and development of fused deposition modeling (FDM) 3D-Printed Orthotic Insole by using gyroid structure. Journal of the mechanical behavior of biomedical materials. **145**, 106005 (2023).
17. Shaikh, S., Jamdade, B. & Chanda, A. Effects of Customized 3D-Printed Insoles in Patients with Foot-Related Musculoskeletal Ailments-A Survey-Based Study. Prosthesis. **5**, 550-561 (2023).
18. Singh, R. et al., Multi-Material Additive Manufacturing of Sustainable Innovative Materials and Structures. Polymers. **11**(1), 62 (2019).

19. Cavalcanti, D.K.K. et al., Recent advances in adhesive bonding of 3D-printed parts and methods to increase their mechanical performance. Annals of “Dunarea de Jos” University of Galati. Fascicle XII, Welding Equipment and Technology. **34**, 17-24 (2023).
20. Mahmud, M. S., Mkawe & P., Islam. Multi-material additive manufacturing for integrated electromechanical systems. American Journal of Interdisciplinary Studies. **4**, 52-79 (2023).
21. Ettayan, H., Abdous, I., Ouballouch, A. & Boutahar, L. Review on multi-material 3D printing via FDM: insights into mechanical performance and printing parameters. Science and Engineering. **133**(2), 49-63 (2025).
22. Chen, C. H., Cheng, Y. H., Chen, S. H., Chuang, A.C. & Chen, J. P. Functional Hyaluronic Acid-Polylactic Acid/Silver Nanoparticles Core-Sheath Nanofiber Membranes for Prevention of Post-Operative Tendon Adhesion. International Journal of Molecular Sciences. **22**(16), 8781 (2021).
23. Naqi, A., Swain, Z. & Mackay, M. Dual material fused filament fabrication via core–shell die design. ACS Applied Polymer Materials. **5**, 2481-2489 (2023).
24. Wei, Q. Y. et al., Fabrication of PLA/CB composites with excellent electrical conductivity and stiffness-ductility balance based on coupling extensional stress with thermal field. Composites Part A: Applied Science and Manufacturing. **169**, 107516 (2023).
25. Papavasileiou, A. V. et al. Unraveling the Versatility of Carbon Black–Polylactic Acid (CB/PLA) 3D-Printed Electrodes via Sustainable Electrochemical Activation. Small Methods. **9**(9), 2402214 (2025).
26. Senthies, T., Senthil, P. & Prakash, C. Application of 3D printed PLA-carbon black conductive polymer composite in solvent sensing. Materials Research Express. **6**, (2019).
27. Park, Y. & Lee, S. Analysis of Fe/PLA composite filament structure for 3D Printing and extrudability. Journal of Defense Quality Study. **5**(1), 65-77 (2023).
28. Amirov, A. et al. 3D Printing of PLA/Magnetic Ferrite Composites: Effect of filler particles on magnetic properties of filament. Processes. **10**(11), 2412 (2022).
29. Moradi, M. et al. Simultaneous FDM 4D printing and magnetizing of iron-filled polylactic acid polymers. Journal of Magnetism and Magnetic Materials. **568**, 170425 (2023).
30. Kantaros, A., Soulis, E., Petrescu, F.I.T. & Ganetsos, T. Advanced Composite Materials Utilized in FDM/FFF 3D Printing Manufacturing Processes: The Case of Filled Filaments. Materials. **16**(18), 6210 (2023).
31. Park, S., Shou, W., Makatura, L., Matusik, W. & Fu., K. K. 3D printing of polymer composites: Materials, processes, and applications. Matter. **5**(1), 43-76 (2022).
32. Leigh, S. J., Bradley, R. J., Purssell, C. P., Billson, D. R. & Hutchins, D. A. A simple, low-cost conductive composite material for 3D printing of electronic sensors. PloS one. **7**(11), e49365 (2012).
33. Huber, C. et al. Additive manufactured and topology optimized passive shimming elements for permanent magnetic systems. Scientific Reports. **8**(1), 14651 (2018).
34. Moradi, M. et al., Simultaneous FDM 4D printing and magnetizing of iron-filled polylactic acid polymers. Journal of Magnetism and Magnetic Materials. **568**, 170425 (2023).
35. Chowdhury, D., Jung, I. & Lee, S. Analysis of 3D-printed longitudinal flatfoot pads with lattice structures using various microfoaming filament. Scientific Reports. **16**(5066), (2026).

Acknowledgements

This work was supported by the National Research Foundation of Korea(NRF) grant funded by the Ministry of Science and ICT of Korea government(MSIT) (No. RS-2025-16064466).

Author contributions

S.L. conceived and designed the research; A.I.J. proceeded with the 3D printing process, characterization of 3D-printed composite structures, integrated insoles, and wrote the manuscript; I.J. assisted with data organization, revised the manuscript, and provided valuable feedback on the interpretation of the results and discussion. S.L. developed the method and provided feedback on the experimental results and discussion. All authors reviewed the manuscript and agreed to its submission.

Funding

This work was supported by the National Research Foundation of Korea(NRF) grant funded by the Ministry of Science and ICT of Korea government(MSIT) (No. RS-2025-16064466).